Multi-Axis Resonant Filter Design using Frequency Response Data applied to Industrial Scan Stage

Masahiro Mae, *Member, IEEE*, Wataru Ohnishi, *Member, IEEE*, Hiroshi Fujimoto, *Fellow, IEEE*, and Koichi Sakata

***Abstract*—Disturbance rejection of the high-precision scan stages is important in industrial lithography equipment. The aim of this article is to develop an optimization method for designing multi-axis resonant filters, that enhance the disturbance rejection performance in scanning motion. The developed optimization method explicitly defines resonant filters in structured representation and formulates the data-driven convex optimization problem. The method enables the multi-axis resonant filter design with iterative convex optimization using the frequency response data of the six-degree-of-freedom experimental setup. Experimental results on the industrial large-scale high-precision scan stage demonstrate the performance improvement of the disturbance rejection in the scanning motion using the optimized resonant filters.**

***Index Terms*—Convex optimization, data-driven design, disturbance rejection, frequency response, loop shaping, multi-input multi-output (MIMO) system, resonant filter.**

I. Introduction

DISTURBANCE rejection in scanning motion has an important role in the product quality of semiconductors and flat panel displays (FPD) in lithography equipment [1], [2]. The disturbance comes from several kinds of sources, such as electrical or mechanical systems around the scanner in several frequencies, and it is difficult to model the disturbance sources in actual systems explicitly. The feedback controller is usually used for disturbance rejection in the two-degree-of-freedom (2-DOF) control scheme. The challenge is how to design the feedback controller considering the disturbance frequency characteristics. The structured definition of the feedback controller is also important in the physical meaning of interpretability and intuitive tuning of on-site control engineers.

Manuscript received 19 January 2024; revised 26 March 2024; accepted 10 May 2024. This work was supported by JSPS KAKENHI under Grant 21J13196 and Grant 23K19116. Recommended by Technical Editor M. Xin and Senior Editor Q. Zou. *(Corresponding author: Masahiro Mae.)*

Masahiro Mae, Wataru Ohnishi, and Hiroshi Fujimoto are with The University of Tokyo, Tokyo 113-8656, Japan (e-mail: mmae@ieee.org; ohnishi@ieee.org; fujimoto@k.u-tokyo.ac.jp).

Koichi Sakata is with Nikon Corporation, Yokohama 244-8533, Japan (e-mail: koichi.sakata@nikon.com).

Color versions of one or more figures in this article are available at https://doi.org/10.1109/TMECH.2024.3402555.

Digital Object Identifier 10.1109/TMECH.2024.3402555

The data-driven design method [3], [4], [5], such as using the frequency response data is one of the solutions for uncertain disturbances without modeling. It also has an advantage in multi-input multi-output (MIMO) systems because of the difficulty of modeling the interaction between each axis compared to single-input single-output (SISO) systems. The challenge in data-driven design is the convex formulation of the optimization problem because the non-convex optimization problem is difficult to guarantee monotonic convergence and it could take a long time for the optimization calculation in practice.

The data-driven feedback controller design methods with the convex optimization have been developed using the sequential linearization with the concave–convex procedure [6] for designing PID controller [7], [8], FIR filter [9], decoupling of MIMO systems [10], mechanical resonance cancellation [11], disturbance observer [12], [13], and peak filter [14].

Although several data-driven feedback controller design methods have been developed, the multi-axis disturbance rejection in several frequencies has not been fully addressed yet, and there is a gap between the theory of numerical optimization and the actual implementation for performance improvement in complex MIMO industrial systems. The aim of this article is to develop a new approach for the multi-axis disturbance rejection in several frequencies during scanning motion using structured feedback controllers designed by convex optimization. As a consequence, the developed approach is applied to the industrial MIMO large-scale high-precision scan stage, and performance improvement is experimentally validated. The only preliminary result is presented in the previous study [15] and the approach is theoretically improved, generalized, and successfully implemented in the actual industrial scan stage in this article.

The main contributions of this article are as follows.

Contribution 1: The optimization problem of multi-axis resonant filter design using frequency response data is formulated with structured representation and phase stabilization.

Contribution 2: The multi-axis resonant filter design problem is solved by iterative convex optimization with the objective function of the MIMO performance evaluation.

Contribution 3: The performance of the designed multi-axis resonant filters is experimentally validated in the industrial MIMO large-scale high-precision scan stage.

The rest of this article is organized as follows. In Section II, the control problem with the experimental setup and the

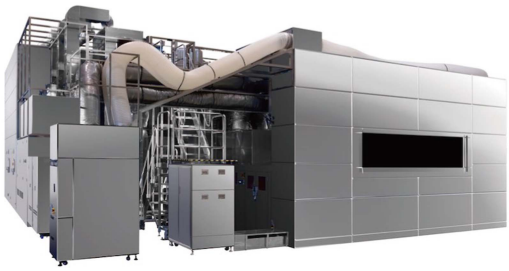

Fig. 1. Experimental setup of FPD lithography system [17].

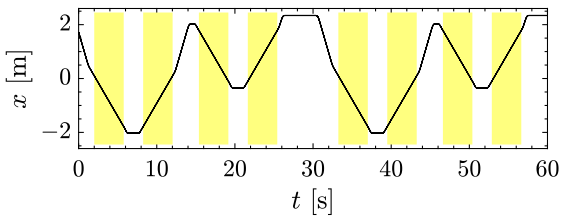

Fig. 2. Scan trajectory of translation along the x-axis. The scan stage moves through 8 scan regions (■) at the same scanning motion. The scanning velocity of translation along the x-axis is set to 0.5m/s.

designed resonant filter is formulated. In Section III, the multi-axis resonant filter design for the MIMO system is formulated, constituting Contribution 1. In Section IV, the resonant filter design problem is solved in iterative convex optimization, constituting Contribution 2. In Section V, the optimized resonant filter is experimentally validated in the industrial MIMO large-scale high-precision scan stage, constituting Contribution 3. Finally, Section VI concludes this article.

II. Problem Formulation

The setup of the industrial MIMO large-scale high-precision scan stage is introduced, and the concept of the multi-axis resonant filter design for disturbance rejection is formulated.

A. Experimental Setup

Fig. 1 shows the experimental setup of the industrial FPD lithography system which is used for the production of FPD. In the setup, the MIMO large-scale high-precision scan stage is implemented and it has 6-DOFs $(x, y, \theta_z, z, \theta_x, \theta_y)$. The 6-DOF stage is supported by the air bearing against gravity and friction, actuated by voice coil motors and linear motors, and measured by laser displacement sensors and linear encoders. The main scan stroke is the translation along the x-axis. The scanning motion is conducted in 8 scan regions shown in Fig. 2. The stage is moving with a constant velocity of 0.5 m/s in scan regions.

The open-loop frequency response data are given for the setup with pre-designed decentralized feedback controllers which consist of PID controllers, disturbance observers, phase lead filters, and notch filters. The open-loop frequency response data are acquired by the system identification using the chirp signal excitation. The Bode magnitude plot of the open-loop frequency response data shown in Fig. 3 is defined as

$$\boldsymbol{G}(\mathrm{j}\omega_{k_f}) = G_{(k_y,k_u)}(\mathrm{j}\omega_{k_f}) \tag{1}$$

where $k_u, k_y \in \{x, y, \theta_z, z, \theta_x, \theta_y\}$ are the indices of inputs and outputs, and the numbers of the input and the output are $n_u = n_y = 6$. The index of frequency response data is $k_f = 1, \ldots, n_f$. Note that the variation of the controlled system can be used as the set of the frequency response data for robustness. The details can be seen in [16].

The 6-DOF controlled system is shown in Fig. 4. In this article, the decentralized multi-axis resonant filters $\boldsymbol{F}$ are designed to reject the disturbance $\boldsymbol{d}$, and are defined as

$$\boldsymbol{F}(\mathrm{j}\omega_{k_f}, \boldsymbol{\rho}) = \mathrm{diag}(F_{k_y}(\mathrm{j}\omega_{k_f}, \boldsymbol{\rho}_{k_y})) \tag{2}$$

where the tuning parameters are $\boldsymbol{\rho} = [\boldsymbol{\rho}_x, \ldots, \boldsymbol{\rho}_{\theta_y}]$.

B. Disturbance Rejection with Multi-Axis Resonant Filters

The resonant filter has high-gained characteristics at the designed resonance frequency and effectively rejects the disturbance at the same frequency as explained in an internal model principle [18]. In the decentralized resonant filter for the MIMO controlled system, resonant filters in each axis are shown in Fig. 5 and are defined as

$$F_{k_y}(\mathrm{j}\omega_{k_f}, \boldsymbol{\rho}_{k_y}) = 1 + \sum_{k_r=1}^{n_{r,k_y}} \frac{\rho_{k_y,(k_r,2)}(\mathrm{j}\omega_{k_f})^2 + \rho_{k_y,(k_r,1)}(\mathrm{j}\omega_{k_f})}{(\mathrm{j}\omega_{k_f})^2 + 2\zeta_{r,k_y,k_r}\omega_{r,k_y,k_r}(\mathrm{j}\omega_{k_f}) + \omega^2_{r,k_y,k_r}} \tag{3}$$

where the number of resonant filter in each axis is n_{r,k_y} and the index of the resonant filters is $k_r = 1, \ldots, n_{r,k_y}$. The tuning parameters, the resonance frequency, and the damping coefficient in each axis are $\rho_{k_y,(k_r,:)}$, ω_{r,k_y,k_r}, and ζ_{r,k_y,k_r}.

The problem addressed in this article is the design of the decentralized multi-axis resonant filters with respect to the following requirements.

Requirement 1: The resonant filter is designed in structured representation in which the parameters have physical meaning.

Requirement 2: The resonant filter is designed by the data-driven method in which the frequency response data are directly used and the parametric model is not needed.

Requirement 3: Convex optimization is used for designing the resonant filter in the MIMO system.

In this article, the optimization method is developed to satisfy these requirements.

III. Formulation of Multi-Axis Resonant Filter Design using Frequency Response Data

In this section, the design method of multi-axis resonant filters is formulated. First, the objective function is designed as the error frequency spectrum evaluation, and the constraints are defined in gain and phase stabilization conditions. The initial condition of the optimization is designed by the pre-existing approach of a resonant filter with stable resonant modes. It results in Contribution 1.

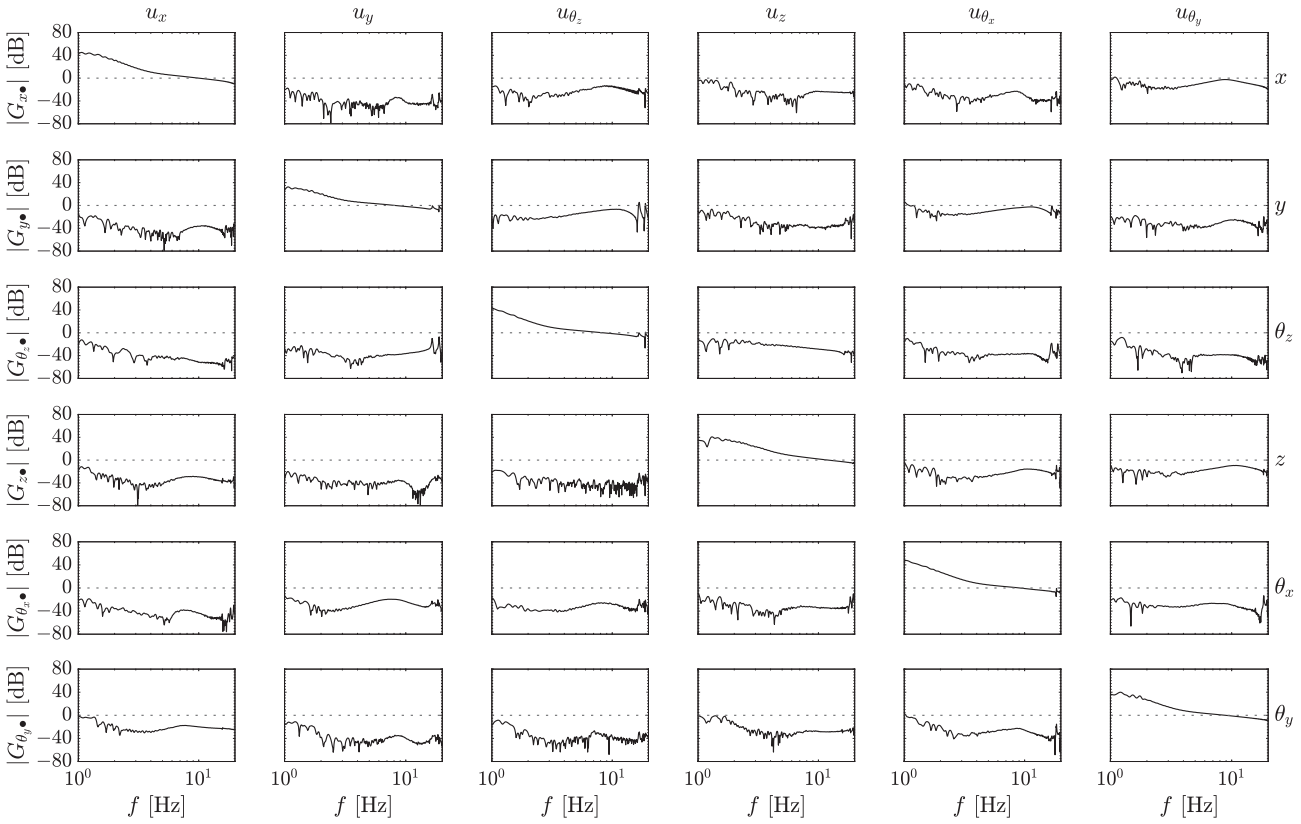

Fig. 3. Bode magnitude plot of open-loop frequency response in the 6-DOF experimental setup.

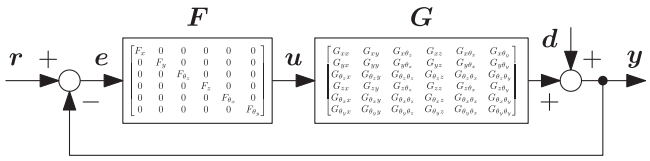

Fig. 4. Block diagram of 6-DOF controlled system.

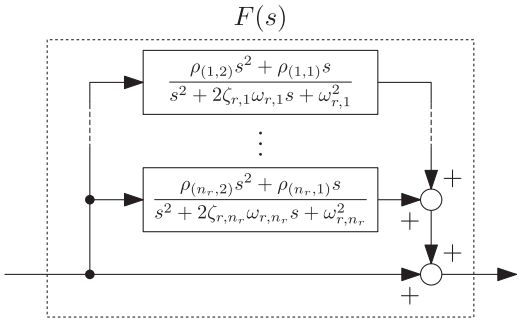

Fig. 5. Block diagram of resonant filters in each axis.

A. Objective Function to Minimize Error Frequency Spectrum

The objective function to optimize multi-axis resonant filters is designed to minimize the error. The challenge of the objective function design is the integrated performance evaluation of multiple axes and multiple scanning regions.

The error frequency spectrum matrix without the resonant filter is measured in the pre-experiment and is defined as

$$\boldsymbol{E}_0(\mathrm{j}\omega_{k_f}) = \begin{bmatrix} \boldsymbol{e}_{0,1}(\mathrm{j}\omega_{k_f}) & \cdots & \boldsymbol{e}_{0,n_e}(\mathrm{j}\omega_{k_f}) \end{bmatrix} \tag{4}$$

where $k_e = 1, \ldots, n_e$ is the index of the scanning regions. The error frequency spectrum in each scanning region $\boldsymbol{e}_{0,k_e}(\mathrm{j}\omega_{k_f}) \in \mathbb{C}^{n_y \times 1}$ is defined as

$$\boldsymbol{e}_{0,k_e}(\mathrm{j}\omega_{k_f}) = \begin{bmatrix} e_{0,k_e,1}(\mathrm{j}\omega_{k_f}) & \cdots & e_{0,k_e,n_y}(\mathrm{j}\omega_{k_f}) \end{bmatrix}^{\mathsf{T}}. \tag{5}$$

From the reproducible error frequency spectrum matrix, the disturbance frequency spectrum matrix is assumed to be invariant for the controller design and is given by

$$\boldsymbol{D}(\mathrm{j}\omega_{k_f}) = \boldsymbol{S}_0^{-1}(\mathrm{j}\omega_{k_f})\boldsymbol{E}_0(\mathrm{j}\omega_{k_f}) \tag{6}$$

where the sensitivity function matrix is $\boldsymbol{S}_0(\mathrm{j}\omega_{k_f}) = (\boldsymbol{I} + \boldsymbol{G}(\mathrm{j}\omega_{k_f}))^{-1} \in \mathbb{C}^{n_y \times n_y}$ with the open-loop frequency response data $\boldsymbol{G}(\mathrm{j}\omega_{k_f})$ and an identity matrix $\boldsymbol{I} \in \mathbb{R}^{n_y \times n_y}$. The element of the disturbance frequency spectrum matrix is defined as

$$\boldsymbol{D}(\mathrm{j}\omega_{k_f}) = \begin{bmatrix} \boldsymbol{d}_1(\mathrm{j}\omega_{k_f}) & \cdots & \boldsymbol{d}_{n_e}(\mathrm{j}\omega_{k_f}) \end{bmatrix} \tag{7}$$

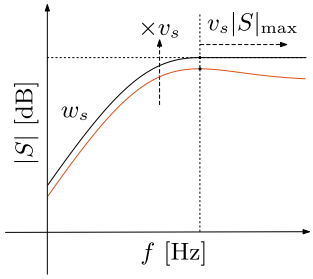

Fig. 6. Constraints of sensitivity function in Bode magnitude plot.

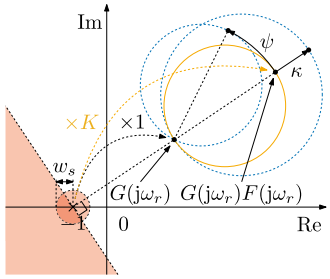

Fig. 7. Vector locus with resonant filter and robust stability condition.

where the disturbance frequency spectrum in each scanning region $\boldsymbol{d}_{k_e}(\mathrm{j}\omega_{k_f}) \in \mathbb{C}^{n_y \times 1}$ is defined as

$$\boldsymbol{d}_{k_e}(\mathrm{j}\omega_{k_f}) = \begin{bmatrix} d_{k_e,1}(\mathrm{j}\omega_{k_f}) & \cdots & d_{k_e,n_y}(\mathrm{j}\omega_{k_f}) \end{bmatrix}^{\mathsf{T}}. \quad (8)$$

The error frequency spectrum matrix with the designed resonant filter is given by

$$\boldsymbol{E}(\mathrm{j}\omega_{k_f}, \boldsymbol{\rho}) = \boldsymbol{S}(\mathrm{j}\omega_{k_f}, \boldsymbol{\rho})\boldsymbol{D}(\mathrm{j}\omega_{k_f}) \quad (9)$$

where the sensitivity function matrix is $\boldsymbol{S}(\mathrm{j}\omega_{k_f}, \boldsymbol{\rho}) = (\boldsymbol{I} + \boldsymbol{G}(\mathrm{j}\omega_{k_f})\boldsymbol{F}(\mathrm{j}\omega_{k_f}, \boldsymbol{\rho}))^{-1} \in \mathbb{C}^{n_y \times n_y}$ with the designed resonant filter $\boldsymbol{F}(\mathrm{j}\omega_{k_f}, \boldsymbol{\rho})$. In the MIMO systems, the unit of each output is different in many actual applications, such as translation and pitching. Therefore, from (9), the normalized error frequency spectrum matrix is given by

$$\boldsymbol{W}^{-1}\boldsymbol{E}(\mathrm{j}\omega_{k_f}, \boldsymbol{\rho}) = \boldsymbol{W}^{-1}(\boldsymbol{I} + \boldsymbol{G}(\mathrm{j}\omega_{k_f})\boldsymbol{F}(\mathrm{j}\omega_{k_f}, \boldsymbol{\rho}))^{-1}\boldsymbol{D}(\mathrm{j}\omega_{k_f}) \quad (10)$$

where the scaling matrix is $\boldsymbol{W} \in \mathbb{R}^{n_y \times n_y}$. In the optimization calculation, the norm of the normalized error frequency spectrum matrix can be used to minimize error.

B. Constraints of Stability Condition

The gain stability condition shown in Fig. 6 is defined as

$$|w_{s,k_y}(\mathrm{j}\omega_{k_f})| - \left|1 + G_{(k_y,k_y)}(\mathrm{j}\omega_{k_f})F_{k_y}(\mathrm{j}\omega_{k_f}, \boldsymbol{\rho})\right| \leq 0 \quad (11)$$

where the weighting function of the upper bound gain in the sensitivity function is $w_{s,k_y}(\mathrm{j}\omega_{k_f})$. Although the constraint of the sensitivity function is commonly used for the frequency response data-based design, the stability cannot be guaranteed only with the gain stability condition in the use of a controller that changes the gain and phase with resonant modes, and the phase stability condition is introduced. The phase stability condition [16] shown in Fig. 7 is defined as

$$\begin{aligned} -\frac{\pi}{2} \leq \angle\left(1 + G_{(k_y,k_y)}(\mathrm{j}\omega_{k_f})F_{k_y}(\mathrm{j}\omega_{k_f}, \boldsymbol{\rho})\right) \\ - \angle\left(1 + G_{(k_y,k_y)}(\mathrm{j}\omega_{k_f})\right) \leq \frac{\pi}{2}. \end{aligned} \quad (12)$$

The phase stability condition represents that the vector locus with the resonant filter is between the angle $\pm 90^\circ$ from the angle with the origin of $(-1, \mathrm{j}0)$ without resonant filters. By integrating the gain and phase stabilization conditions, the vector locus with resonant filters must be on the same side against $(-1, \mathrm{j}0)$ and at the outside of the modulus margin.

C. Resonant Filter Design with Stable Resonant Mode

For the initial condition with stable resonant modes [19], the resonant mode of the designed resonant filter is defined as

$$F_r(s) = \frac{\kappa s^2 + \kappa\psi s}{s^2 + 2\zeta_r\omega_r s + \omega_r^2} \quad (13)$$

where the tuning parameters are the gain κ and the phase ψ. The resonance frequency ω_r and the damping coefficient ζ_r are usually pre-defined by the shape of the error frequency spectrum. The parameters in this representation have physical meaning and satisfy Requirement 1.

The initial resonant filters are designed as K times larger gain at the resonance frequency ω_r and the vector locus recedes from $(-1, \mathrm{j}0)$ with a resonance circle, as shown in Fig. 7. The parameter K is tuned by the users based on the error frequency spectrum. In this condition, the parameter ψ is given by

$$\psi = \omega_r \frac{\mathrm{Re}\{T^{-1}(\mathrm{j}\omega_r)\}}{\mathrm{Im}\{T^{-1}(\mathrm{j}\omega_r)\}} \quad (14)$$

where the complementary sensitivity function at the resonance frequency ω_r is given by $T(\mathrm{j}\omega_r) = \frac{G(\mathrm{j}\omega_r)}{1+G(\mathrm{j}\omega_r)}$. The parameter κ can be derived geometrically [19] and is given by

$$\begin{aligned} \kappa &= \frac{\pm 2\zeta_r\omega_r}{\sqrt{\psi^2 + \omega_r^2}}(K-1)|T^{-1}(\mathrm{j}\omega_r)| \\ \text{when} \quad \angle T^{-1}(\mathrm{j}\omega_r) &= \mathrm{atan2}\left(\frac{\pm\omega_r}{\pm\psi}\right) \end{aligned} \quad (15)$$

where the order of plus and minus corresponds to each other.

Using these initial conditions for optimization, the designed resonant filters in each axis are linearly parameterized in tuning parameters of the numerator and are defined as

$$F_{k_y}(\mathrm{j}\omega_{k_f}, \boldsymbol{\rho}_{k_y}) = \boldsymbol{\rho}_{k_y}^{\mathsf{T}}\boldsymbol{\phi}_{k_y}(\mathrm{j}\omega_{k_f})$$

$$= \begin{bmatrix} 1 \\ \rho_{k_y,(1,1)} \\ \rho_{k_y,(1,2)} \\ \vdots \\ \rho_{k_y,(n_{r,k_y},1)} \\ \rho_{k_y,(n_{r,k_y},2)} \end{bmatrix}^{\mathsf{T}}$$

$$\cdot \begin{bmatrix} 1 \\ \dfrac{(\mathrm{j}\omega_{k_f})}{(\mathrm{j}\omega_{k_f})^2 + 2\zeta_{r,k_y,1}\omega_{r,k_y,1}(\mathrm{j}\omega_{k_f}) + \omega_{r,k_y,1}^2} \\ \dfrac{(\mathrm{j}\omega_{k_f})^2}{(\mathrm{j}\omega_{k_f})^2 + 2\zeta_{r,k_y,1}\omega_{r,k_y,1}(\mathrm{j}\omega_{k_f}) + \omega_{r,k_y,1}^2} \\ \vdots \\ \dfrac{(\mathrm{j}\omega_{k_f})}{(\mathrm{j}\omega_{k_f})^2 + 2\zeta_{r,k_y,n_{r,k_y}}\omega_{r,k_y,n_{r,k_y}}(\mathrm{j}\omega_{k_f}) + \omega_{r,k_y,n_{r,k_y}}^2} \\ \dfrac{(\mathrm{j}\omega_{k_f})^2}{(\mathrm{j}\omega_{k_f})^2 + 2\zeta_{r,k_y,n_{r,k_y}}\omega_{r,k_y,n_{r,k_y}}(\mathrm{j}\omega_{k_f}) + \omega_{r,k_y,n_{r,k_y}}^2} \end{bmatrix} \tag{16}$$

where the tuning parameters are $\boldsymbol{\rho}_{k_y} \in \mathbb{R}^{2n_{r,k_y}+1}$.

IV. Optimization of Multi-Axis Resonant Filter

In this section, the optimization approach to design the multi-axis resonant filter is formulated. The MIMO performance is evaluated by the Frobenius norm of the normalized error frequency spectrum matrix. The original non-convex optimization problem is reformulated to the iterative convex optimization problem by the Moore–Penrose inverse and sequential linearization. It results in Contribution 2.

A. Non-Convex Optimization Problem Formulation

From the objective function (10), and the constrains (11) and (12), the optimization problem is formulated as

$$\underset{\boldsymbol{\rho}}{\text{minimize}} \quad \max_{\forall k_f} \|\boldsymbol{W}^{-1}(\boldsymbol{I}+\boldsymbol{G}(\mathrm{j}\omega_{k_f})\boldsymbol{F}(\mathrm{j}\omega_{k_f},\boldsymbol{\rho}))^{-1}\boldsymbol{D}(\mathrm{j}\omega_{k_f})\|_F^2 \tag{17a}$$

$$\text{subject to} \quad {}^{\forall k_f,\forall k_y}$$

$$|w_{s,k_y}(\mathrm{j}\omega_{k_f})| - \left|1 + G_{(k_y,k_y)}(\mathrm{j}\omega_{k_f})F_{k_y}(\mathrm{j}\omega_{k_f},\boldsymbol{\rho})\right| \le 0 \tag{17b}$$

$$-\frac{\pi}{2} \le \angle\left(1 + G_{(k_y,k_y)}(\mathrm{j}\omega_{k_f})F_{k_y}(\mathrm{j}\omega_{k_f},\boldsymbol{\rho})\right) - \angle\left(1 + G_{(k_y,k_y)}(\mathrm{j}\omega_{k_f})\right) \le \frac{\pi}{2} \tag{17c}$$

where the MIMO performance is evaluated as the maximum square Frobenius norm of the normalized error frequency spectrum matrix at each frequency. The optimization problem is formulated by the data-driven design method in which the frequency response data are directly used and satisfy Requirement 2. The challenge is how to formulate a convex optimization problem that satisfies Requirement 3.

B. Objective Function Formulation by Moore–Penrose Inverse

To deal with the non-convex objective function that includes the parameter $\boldsymbol{\rho}$ in the inverse, the Moore–Penrose inverse is applied. The Moore–Penrose inverse of the normalized error frequency spectrum matrix (10) is given by

$$\boldsymbol{E}^{+}(\mathrm{j}\omega_{k_f},\boldsymbol{\rho})\boldsymbol{W} = \boldsymbol{D}^{+}(\mathrm{j}\omega_{k_f})(\boldsymbol{I} + \boldsymbol{G}(\mathrm{j}\omega_{k_f})\boldsymbol{F}(\mathrm{j}\omega_{k_f},\boldsymbol{\rho}))\boldsymbol{W} \tag{18}$$

and the reformulated objective function is given by

$$\underset{\boldsymbol{\rho}}{\text{maximize}} \quad \min_{\forall k_f} \|\boldsymbol{D}^{+}(\mathrm{j}\omega_{k_f})(\boldsymbol{I} + \boldsymbol{G}(\mathrm{j}\omega_{k_f})\boldsymbol{F}(\mathrm{j}\omega_{k_f},\boldsymbol{\rho}))\boldsymbol{W}\|_F^2 \tag{19}$$

where the performance value is evaluated as the minimum square Frobenius norm of the normalized Moore–Penrose inverse error frequency spectrum matrix at each frequency. From the property of the Frobenius norm and the singular value, the objective function becomes the sum of the inverse square singular value of the normalized error frequency spectrum matrix. The difference between (17a) and (19) is that the evaluation of the singular values of the error frequency spectrum matrix is whether the arithmetic mean or the harmonic mean. The linear parameterization for convex optimization is maintained in this formulation. Note that the number of the scanning regions n_e should be greater than or equal to that of the output n_y and satisfying $n_e \ge n_y$ to compute the Moore–Penrose inverse in this matrix order.

The optimization problem is reformulated as

$$\underset{\boldsymbol{\rho}}{\text{maximize}} \quad \gamma \tag{20a}$$

$$\text{subject to} \quad {}^{\forall k_f,\forall k_y}$$

$$\gamma - \|\boldsymbol{D}^{+}(\mathrm{j}\omega_{k_f})(\boldsymbol{I}+\boldsymbol{G}(\mathrm{j}\omega_{k_f})\boldsymbol{F}(\mathrm{j}\omega_{k_f},\boldsymbol{\rho}))\boldsymbol{W}\|_F^2 \le 0 \tag{20b}$$

$$|w_{s,k_y}(\mathrm{j}\omega_{k_f})| - \left|1 + G_{(k_y,k_y)}(\mathrm{j}\omega_{k_f})F_{k_y}(\mathrm{j}\omega_{k_f},\boldsymbol{\rho})\right| \le 0 \tag{20c}$$

$$-\frac{\pi}{2} \le \angle\left(1 + G_{(k_y,k_y)}(\mathrm{j}\omega_{k_f})F_{k_y}(\mathrm{j}\omega_{k_f},\boldsymbol{\rho})\right) - \angle\left(1 + G_{(k_y,k_y)}(\mathrm{j}\omega_{k_f})\right) \le \frac{\pi}{2} \tag{20d}$$

where the objective function (19) is defined in the constraint (20b) with the parameter $\gamma \in \mathbb{R}_0^+$ of the objective function.

C. Iterative Convex Optimization using Sequential Linearization

The constraints of the non-convex optimization problem (20) can be dealt with by a sequential linearization using the concave–convex procedure [6]. The derivatives around the operating point of the current iteration in the variable $\boldsymbol{\rho}$ can be solved by an iterative convex optimization calculation (21) that is shown at the bottom of the next page. Finally, the design procedure is summarized in Algorithm 1. It can be solved in an iterative convex optimization calculation and has an advantage in monotonic convergence to a saddle point or a local optimum. It results in satisfying Requirement 3.

V. Experimental Validation

In this section, the experimental validation is conducted in the industrial MIMO large-scale high-precision scan stage. The MIMO stability analysis is conducted before the implementation. The experimental results demonstrate the scanning performance improvement with the optimized resonant filters. It results in Contribution 3.

Algorithm 1: Multi-axis resonant filter design.

Input: $\boldsymbol{G}(\mathrm{j}\omega), \boldsymbol{E}_0(\mathrm{j}\omega), \boldsymbol{W}, \omega_r, \zeta_r, K, w_s, \gamma_{\mathrm{end}}/\gamma_{\mathrm{end}-1}$
Output: $\boldsymbol{\rho}_{\mathrm{opt}}$
1: obtain $\boldsymbol{\rho}_{\mathrm{ini}}$ from (13)–(16)
2: compute $\boldsymbol{D}(\mathrm{j}\omega)$ from (6)
3: **while** $(\gamma_{k_i}/\gamma_{k_i-1}) \geq (\gamma_{\mathrm{end}}/\gamma_{\mathrm{end}-1})$ **do**
4: $\underset{\boldsymbol{\rho}}{\text{maximize}}\ \ \gamma \quad \text{subject to convex constraints (21)} \ {}^{\forall}{}_{k_f,{}^{\forall},k_y}$
5: **end**

A. Conditions

The 6-DOF experimental setup is shown in Fig. 1 and the stage is moving along the main stroke x-axis with constant velocity 0.5 m/s and the number of the scanning regions is $n_e = 8$, as shown in Fig. 2. The number of frequency response data points is $n_f = 1000$ and the data points are arranged at linearly even intervals in the range from 1 to 20 Hz. The Bode magnitude plot of the open-loop frequency response data $\boldsymbol{G}(\mathrm{j}\omega_{k_f})$ is shown in Fig. 3.

The resonance frequency ω_r of the designed resonant filter is pre-defined by the shape of the inverse disturbance spectrum, as shown in Fig. 8, and the damping coefficient is set to $\zeta_r = 0.01$. The initial resonant filter is designed with stable resonant modes using the approach presented in [19]. The initial resonant filters are designed as $K = 2$ times larger gain at the resonance frequency ω_r and the vector locus recedes from $(-1, \mathrm{j}0)$ using (14) and (15). Note that the resonant filters are designed in $(x, z, \theta_x, \theta_y)$-axes because (y, θ_z)-axes are originally too high sensitivity peak before designing the resonant filters and not afford to design additional resonant filters with robustness in the actual implementation. The scaling matrix $\boldsymbol{W}$ is designed in the diagonal matrix with the root mean square error of 8 scan regions for each axis in the pre-experiment without the resonant filter.

The gain stabilization condition is designed by a data-driven approach with the scaled sensitivity function without the resonant filter as shown in Fig. 6. The weighting function of the sensitivity function is given by

$$w_{s,k_y}(\mathrm{j}\omega_{k_f}) = v_s \times \begin{cases} (1 + G_{(k_y,k_y)}(\mathrm{j}\omega_{k_f})) & (\omega_{k_f} \leq \omega_{k_y,s_{\max}}) \\ (1 + G_{(k_y,k_y)}(\mathrm{j}\omega_{k_y,s_{\max}})) & (\omega_{k_f} > \omega_{k_y,s_{\max}}) \end{cases} \tag{22}$$

$$\gamma - \sum_{k_e,k_y} \left[2|\boldsymbol{D}^{+}(\mathrm{j}\omega_{k_f})(\boldsymbol{I} + \boldsymbol{G}(\mathrm{j}\omega_{k_f})\boldsymbol{F}(\mathrm{j}\omega_{k_f}, \boldsymbol{\rho}_{(k_i-1)}))\boldsymbol{W}|_{(k_e,k_y)} \mathrm{Re}\left\{ \frac{(\boldsymbol{D}^{+}(\mathrm{j}\omega_{k_f})(\boldsymbol{I} + \boldsymbol{G}(\mathrm{j}\omega_{k_f})\boldsymbol{F}(\mathrm{j}\omega_{k_f}, \boldsymbol{\rho}_{(k_i-1)}))\boldsymbol{W})^{*}_{(k_e,k_y)}}{|\boldsymbol{D}^{+}(\mathrm{j}\omega_{k_f})(\boldsymbol{I} + \boldsymbol{G}(\mathrm{j}\omega_{k_f})\boldsymbol{F}(\mathrm{j}\omega_{k_f}, \boldsymbol{\rho}_{(k_i-1)}))\boldsymbol{W}|_{(k_e,k_y)}} \right.\right.$$
$$\left.\left. \times (\boldsymbol{D}^{+}(\mathrm{j}\omega_{k_f})(\boldsymbol{I} + \boldsymbol{G}(\mathrm{j}\omega_{k_f})\boldsymbol{F}(\mathrm{j}\omega_{k_f}, \boldsymbol{\rho}_{k_i}))\boldsymbol{W})_{(k_e,k_y)} \right\} - |\boldsymbol{D}^{+}(\mathrm{j}\omega_{k_f})(\boldsymbol{I} + \boldsymbol{G}(\mathrm{j}\omega_{k_f})\boldsymbol{F}(\mathrm{j}\omega_{k_f}, \boldsymbol{\rho}_{(k_i-1)}))\boldsymbol{W}|^2_{(k_e,k_y)} \right] \leq 0 \tag{21a}$$

$$|w_{s,k_y}(\mathrm{j}\omega_{k_f})| - \mathrm{Re}\left\{ \frac{(1 + G_{(k_y,k_y)}(\mathrm{j}\omega_{k_f})F_{k_y}(\mathrm{j}\omega_{k_f}, \boldsymbol{\rho}_{(k_i-1)}))^{*}}{|1 + G_{(k_y,k_y)}(\mathrm{j}\omega_{k_f})F_{k_y}(\mathrm{j}\omega_{k_f}, \boldsymbol{\rho}_{(k_i-1)})|} (1 + G_{(k_y,k_y)}(\mathrm{j}\omega_{k_f})F_{k_y}(\mathrm{j}\omega_{k_f}, \boldsymbol{\rho}_{k_i})) \right\} \leq 0 \tag{21b}$$

$$\mp \left(\mathrm{atan2}\left(\frac{\mathrm{Im}(1 + G_{(k_y,k_y)}(\mathrm{j}\omega_{k_f})F_{k_y}(\mathrm{j}\omega_{k_f}, \boldsymbol{\rho}_{(k_i-1)}))}{\mathrm{Re}(1 + G_{(k_y,k_y)}(\mathrm{j}\omega_{k_f})F_{k_y}(\mathrm{j}\omega_{k_f}, \boldsymbol{\rho}_{(k_i-1)}))} \right) \right.$$
$$\left. + \frac{\begin{array}{r}\mathrm{Re}(1 + G_{(k_y,k_y)}(\mathrm{j}\omega_{k_f})F_{k_y}(\mathrm{j}\omega_{k_f}, \boldsymbol{\rho}_{(k_i-1)}))\mathrm{Im}(1 + G_{(k_y,k_y)}(\mathrm{j}\omega_{k_f})F_{k_y}(\mathrm{j}\omega_{k_f}, \boldsymbol{\rho}_{k_i})) \\ -\mathrm{Im}(1 + G_{(k_y,k_y)}(\mathrm{j}\omega_{k_f})F_{k_y}(\mathrm{j}\omega_{k_f}, \boldsymbol{\rho}_{(k_i-1)}))\mathrm{Re}(1 + G_{(k_y,k_y)}(\mathrm{j}\omega_{k_f})F_{k_y}(\mathrm{j}\omega_{k_f}, \boldsymbol{\rho}_{k_i}))\end{array}}{\left|1 + G_{(k_y,k_y)}(\mathrm{j}\omega_{k_f})F_{k_y}(\mathrm{j}\omega_{k_f}, \boldsymbol{\rho}_{(k_i-1)})\right|^2} \right)$$
$$\pm \mathrm{atan2}\left(\frac{\mathrm{Im}(1 + G_{(k_y,k_y)}(\mathrm{j}\omega_{k_f}))}{\mathrm{Re}(1 + G_{(k_y,k_y)}(\mathrm{j}\omega_{k_f}))} \right) - \frac{\pi}{2} \leq 0$$
$$\text{when} \quad \pm \mathrm{Re}(1 + G_{(k_y,k_y)}(\mathrm{j}\omega_{k_f})) \geq 0 \tag{21c}$$

$$\pm \left(\mathrm{atan2}\left(\frac{\mathrm{Im}(1 + G_{(k_y,k_y)}(\mathrm{j}\omega_{k_f})F_{k_y}(\mathrm{j}\omega_{k_f}, \boldsymbol{\rho}_{(k_i-1)}))}{\mathrm{Re}(1 + G_{(k_y,k_y)}(\mathrm{j}\omega_{k_f})F_{k_y}(\mathrm{j}\omega_{k_f}, \boldsymbol{\rho}_{(k_i-1)}))} \right) \right.$$
$$\left. + \frac{\begin{array}{r}\mathrm{Re}(1 + G_{(k_y,k_y)}(\mathrm{j}\omega_{k_f})F_{k_y}(\mathrm{j}\omega_{k_f}, \boldsymbol{\rho}_{(k_i-1)}))\mathrm{Im}(1 + G_{(k_y,k_y)}(\mathrm{j}\omega_{k_f})F_{k_y}(\mathrm{j}\omega_{k_f}, \boldsymbol{\rho}_{k_i})) \\ -\mathrm{Im}(1 + G_{(k_y,k_y)}(\mathrm{j}\omega_{k_f})F_{k_y}(\mathrm{j}\omega_{k_f}, \boldsymbol{\rho}_{(k_i-1)}))\mathrm{Re}(1 + G_{(k_y,k_y)}(\mathrm{j}\omega_{k_f})F_{k_y}(\mathrm{j}\omega_{k_f}, \boldsymbol{\rho}_{k_i}))\end{array}}{\left|1 + G_{(k_y,k_y)}(\mathrm{j}\omega_{k_f})F_{k_y}(\mathrm{j}\omega_{k_f}, \boldsymbol{\rho}_{(k_i-1)})\right|^2} \right)$$
$$\mp \mathrm{atan2}\left(\frac{\mathrm{Im}(1 + G_{(k_y,k_y)}(\mathrm{j}\omega_{k_f}))}{\mathrm{Re}(1 + G_{(k_y,k_y)}(\mathrm{j}\omega_{k_f}))} \right) - \frac{\pi}{2} \leq 0$$
$$\text{when} \quad \pm \mathrm{Re}(1 + G_{(k_y,k_y)}(\mathrm{j}\omega_{k_f})) \geq 0. \tag{21d}$$

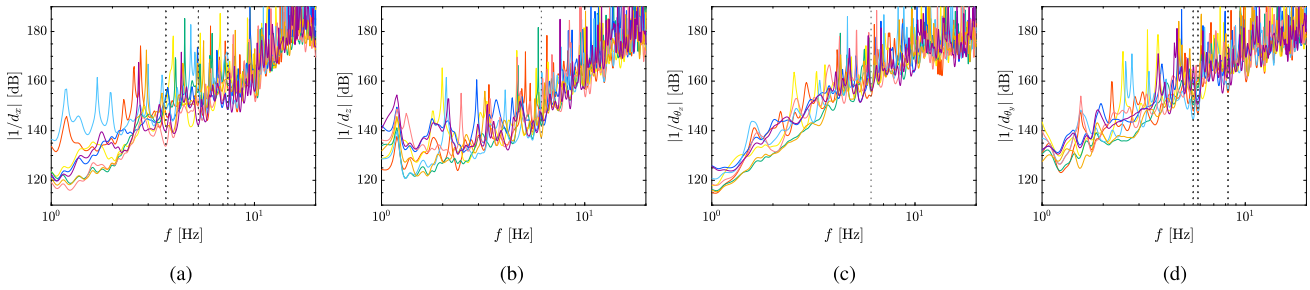

Fig. 8. Inverse disturbance spectrum of 8 scan regions. Vertical black dotted lines (⋯) correspond to resonance frequencies of designed resonant filters. (a) x. (b) z. (c) θ_x. (d) θ_y.

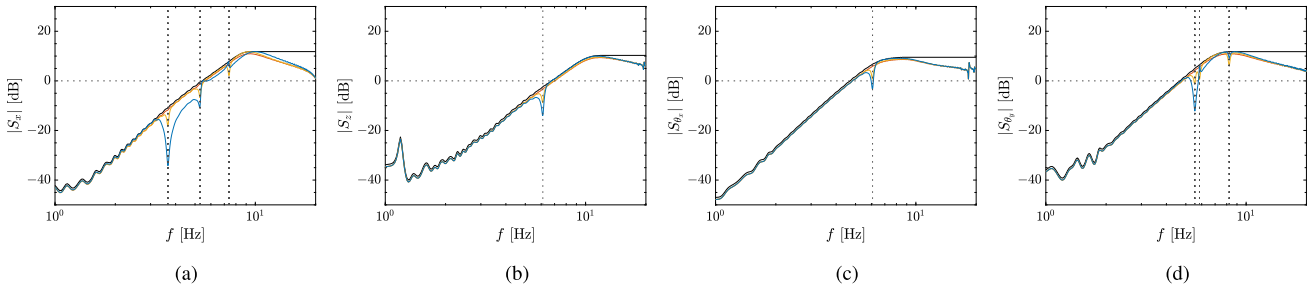

Fig. 9. Bode magnitude plot of SISO sensitivity function without resonant filters (—), with initial resonant filters (—), and with optimized resonant filters (—). Constraints of sensitivity function are shown in (—). Vertical black dotted lines (⋯) correspond to resonance frequencies of designed resonant filters. (a) x. (b) z. (c) θ_x. (d) θ_y.

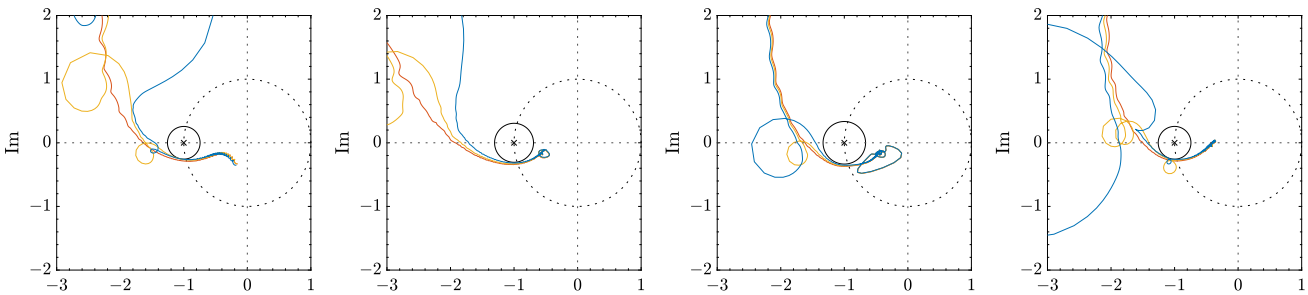

Fig. 10. Nyquist plot without resonant filters (—), with initial resonant filters (—), and with optimized resonant filters (—). Sensitivity peaks are shown in (—). (a) x. (b) z. (c) θ_x. (d) θ_y.

where the scaling parameter is set to $v_s = 1/1.1$ and

$$\min_{\forall k_f} |1 + G_{(k_y,k_y)}(\mathrm{j}\omega_{k_f})| = |1 + G_{(k_y,k_y)}(\mathrm{j}\omega_{k_y,s_{\max}})|. \quad (23)$$

Note that the initial resonant filters do not satisfy this gain stabilization condition although they are designed with stable resonant modes.

The iterative calculation in the optimization is continued until the improvement of the objective function is less than 0.1% set as $\gamma_{\mathrm{end}}/\gamma_{\mathrm{end}-1} = 1.001$. The optimization problem is computed in several minutes by the laptop using MATLAB, YALMIP [20], and MOSEK [21].

B. Optimization Result

The Bode magnitude plot of the sensitivity function in the diagonal SISO open-loop systems without the resonant filters (w/o), with the initial resonant filters (ini), and with the optimized resonant filters (opt) are shown in Fig. 9. It shows that the optimized resonant filters satisfy the constraints of the robust stability condition that is not satisfied by the initial resonant filters.

The Nyquist plot of the diagonal SISO open-loop systems without the resonant filters (w/o), with the initial resonant filters (ini), and with the optimized resonant filters (opt) are shown in Fig. 10. It shows that both the gain and phase of the resonant

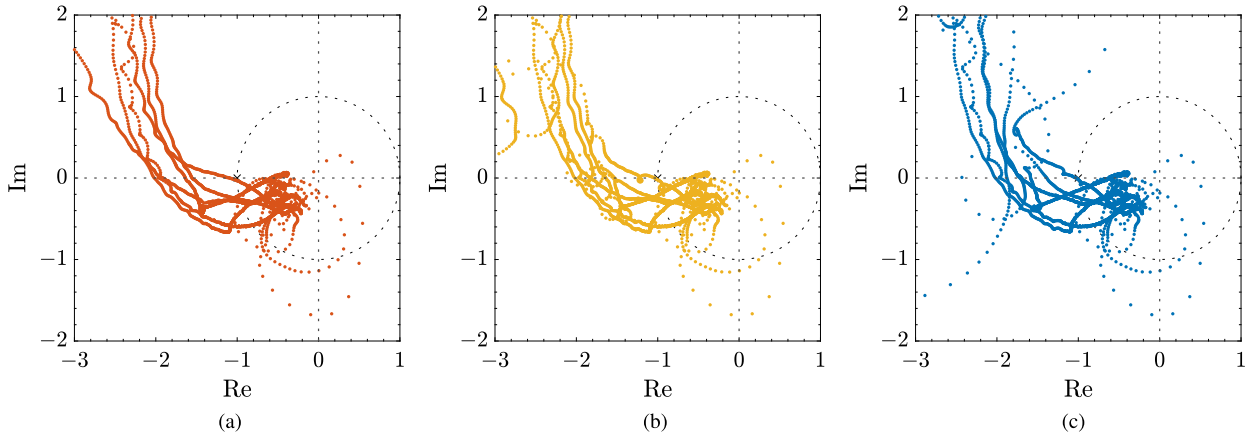

Fig. 11. Eigenvalue loci (a) without resonant filters (w/o), (b) with initial resonant filters (ini), and (c) with optimized resonant filters (opt).

TABLE I
EXPERIMENTAL ROOT MEAN SQUARE ERRORS OF 8 SCAN REGIONS IN 6-DOFS WITHOUT RESONANT FILTERS (W/O), WITH INITIAL RESONANT FILTERS (INI), AND WITH OPTIMIZED RESONANT FILTERS (OPT)

[count]	e_x	e_y	e_{θ_z}	e_z	e_{θ_x}	e_{θ_y}	$\int_t \|\boldsymbol{W}^{-1}\boldsymbol{E}\|_F$
w/o	49	120	28	116	61	75	100 %
ini	88	88	41	111	60	108	104 %
opt	59	65	34	107	48	116	87 %

filters are tuned to improve the disturbance rejection performance by optimization.

C. MIMO Stability Analysis using Eigenvalue Loci

The stability analysis of the closed-loop system with the designed controller is always important in the actual implementation. The challenge is the stability in MIMO systems because the stability condition in SISO systems is not necessary and sufficient for that in MIMO systems. The sufficient condition of MIMO stability, such as using a generalized Gershgorin band in [14] results in conservative controller design. In this article, the eigenvalue loci [22] are used for MIMO stability analysis in necessary and sufficient conditions. Note that the necessary and sufficient condition of MIMO stability includes the computation of eigenvalue and it is difficult to implement in convex optimization. The eigenvalue loci without the resonant filters (w/o), with the initial resonant filters (ini), and with the optimized resonant filters (opt) are shown in Fig. 11. It shows that the MIMO stability condition is satisfied in all cases. Nyquist stability analysis using frequency response data is reliable in linear systems because of no modeling error except for the assumption of dominant linear dynamics. Although the eigenvalue loci are close to $(-1, \mathrm{j}0)$, as shown in Fig. 11, it is because the controllers are designed with less robust margin to satisfy the severe performance requirement. All controllers are successfully implemented in the experimental setup and the scanning performance is validated.

D. Experimental Result

The scanning performance is validated in the last 0.5 s of 8 scan regions as a steady-state scanning error. The experimental time series errors of 8 scan regions in 6-DOFs without resonant filters, with initial resonant filters, and with optimized resonant filters are shown in Fig. 12. From Fig. 12, the experimental root mean square errors of 8 scan regions in 6-DOFs are shown in Table I. From the identity of Parseval's theorem between the time domain signal and the frequency domain signal in square integral, the integral normalized Frobenius norm of the time series error signal matrix of 8 scan regions in 6-DOFs $\int_t \|\boldsymbol{W}^{-1}\boldsymbol{E}\|_F$ is used to evaluate the MIMO performance of each approach. The results show that the MIMO performance with optimized resonant filters outperforms that without resonant filters in 13% and that with initial resonant filters in 17%. The initial resonant filters are designed without considering the MIMO performance and it may worsen the MIMO performance because of the interaction between each axes. The optimized resonant filters are designed with optimization for the gain and phase of the resonant filters to improve the MIMO performance. Note that the root mean square errors with the resonant filters are not improved in all axes but become worse in several axes, such as in x and θ_y axes because of the SISO performance trade-off and the nonlinear interaction dynamics between translation and rotation. Although the controller design using the linear frequency spectrum has a limitation in considering nonlinearity, it is a reasonable linear approximation around the operating points.

The experimental cumulative amplitude spectrum errors of 8 scan regions are shown in Fig. 13. The disturbance rejection performance is improved in z and θ_x axes but high-gained interaction deteriorates low-frequency performance in x and θ_y axes. Note that the final value of the cumulative amplitude spectrum in Fig. 13 is the same as the root mean square error in Table I from the identity of Parseval's theorem.

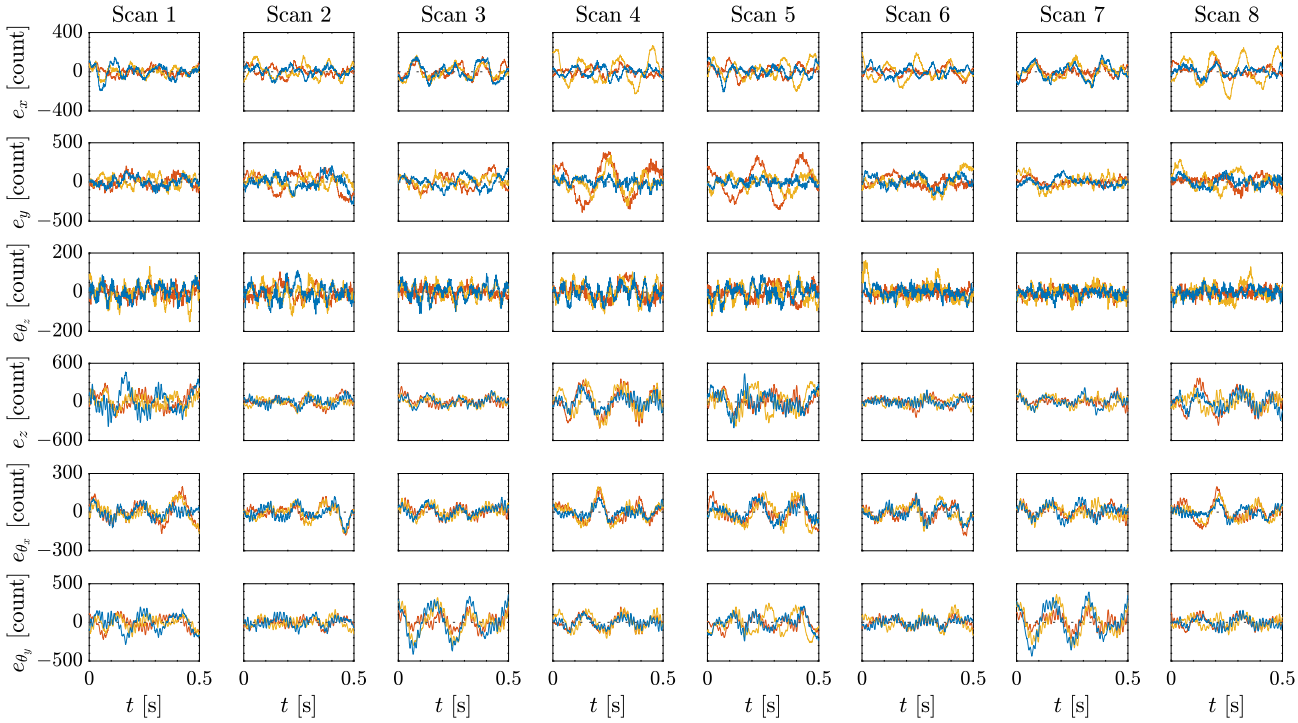

Fig. 12. Experimental time series errors of 8 scan regions in 6-DOFs without resonant filters (—), with initial resonant filters (—), and with optimized resonant filters (—).

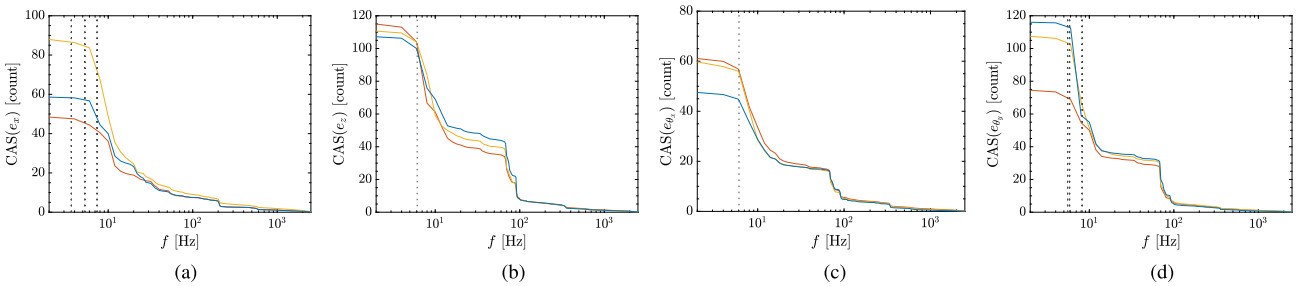

Fig. 13. Experimental cumulative amplitude spectrum (CAS) errors of 8 scan regions from high to low frequency without resonant filters (—), with initial resonant filters (—), and with optimized resonant filters (—). Vertical black dotted lines (⋯) correspond to resonance frequencies of designed resonant filters. (a) x. (b) z. (c) θ_x. (d) θ_y.

VI. Conclusion

The disturbance rejection in the scanning motion has an important role in the lithography equipment. In this article, the decentralized multi-axis resonant filters are formulated in structured representation to compensate for disturbances. The resonant filter design problem is solved by iterative convex optimization. Experiments on the industrial MIMO large-scale high-precision scan stage demonstrate effective disturbance rejection performance with the optimized resonant filters. Ongoing research focuses on global optimization with the initial parameter dependence, nonlinear optimization with the coefficients of the denominator, and total optimization with other pre-designed feedback controllers.

References

[1] M. Heertjes et al., "Control of wafer scanners: Methods and developments," in *Proc. Amer. Control Conf.*, 2020, pp. 3686–3703.

[2] M. Steinbuch, T. Oomen, and H. Vermeulen, "Motion control, mechatronics design, and Moore's law," *IEEJ J. Ind. Appl.*, vol. 2, no. 4, 2021, Art. no. 21006010.

[3] R. de Rozario, A. Fleming, and T. Oomen, "Finite-time learning control using frequency response data with application to a nanopositioning stage," *IEEE/ASME Trans. Mechatron.*, vol. 24, no. 5, pp. 2085–2096, Oct. 2019.

[4] L. Blanken, S. Koekebakker, and T. Oomen, "Multivariable repetitive control: Decentralized designs with application to continuous media flow printing," *IEEE/ASME Trans. Mechatron.*, vol. 25, no. 1, pp. 294–304, Feb. 2020.

[5] E. Kuroda, Y. Maeda, and M. Iwasaki, "Autonomous parameter design for cascade-structure feedback controller based on cooperative optimization method," *IEEJ J. Ind. Appl.*, vol. 10, no. 4, Jul. 2021, Art. no. 20011750.

[6] A. L. Yuille and A. Rangarajan, "The concave–convex procedure," *Neural Computation*, vol. 15, no. 4, pp. 915–936, Apr. 2003.

[7] A. Karimi and G. Galdos, "Fixed-order H infinity controller design for nonparametric models by convex optimization," *Automatica*, vol. 46, no. 8, pp. 1388–1394, Aug. 2010.

[8] S. Boyd, M. Hast, and K. J. Åström, "MIMO PID tuning via iterated LMI restriction," *Int. J. Robust Nonlinear Control*, vol. 26, no. 8, pp. 1718–1731, May 2016.

[9] K. Nakamura, K. Yubai, D. Yashiro, and S. Komada, "Fully parameterized controller design method for high control bandwidth using frequency response data sets," in *Proc. 3rd IEEJ Int. Workshop Sens., Actuation, Motion Control, Optim.*, TT1-1, 2017, pp. 1–6.
[10] S. Shinoda, K. Yubai, D. Yashiro, and J. Hirai, "Multivariable controller design achieving diagonal dominance using frequency response data," *Electron. Commun. Jpn*, vol. 100, no. 10, pp. 12–23, Oct. 2017.
[11] W. Ohnishi, "Data-based feedback controller tuning utilizing collocated and non-collocated sensors," in *Proc. Joint 8th IFAC Symp. Mechatronic Syst. 11th IFAC Symp. Nonlinear Control Syst.*, 2019, pp. 157–162.
[12] X. Wang, W. Ohnishi, and T. Koseki, "Linear matrix inequality based data-driven disturbance observer design: Application to a non-minimum phase motion stage," *IEEJ J. Ind. Appl.*, vol. 11, 2021, Art. no. 21005770.
[13] X. Wang, W. Ohnishi, and T. Koseki, "Frequency response data based disturbance observer design: With application to a nonminimum phase motion stage," *IEEE/ASME Trans. Mechatron.*, vol. 27, no. 6, pp. 5318–5326, Dec. 2022.
[14] M. Mae, W. Ohnishi, H. Fujimoto, K. Sakata, and A. Hara, "Frequency response data-based peak filter design applied to MIMO large-scale high-precision scan stage," *Mechatronics*, vol. 83, 2020, Art. no. 102733.
[15] M. Mae, W. Ohnishi, H. Fujimoto, and K. Sakata, "Frequency response data-based multiple peak filter design applied to high-precision stage in translation and pitching," in *Proc. IEEE 17th Int. Conf. Adv. Motion Control*, 2022, pp. 100–105.
[16] M. Mae, W. Ohnishi, and H. Fujimoto, "Frequency response data-based resonant filter design considering phase stabilization and stroke limitation applied to dual-stage actuator hard disk drives," in *Proc. The 22nd IFAC World Congr.*, 2023, pp. 10614–10619.
[17] Nikon, "FPD lithography systems lineup," 2024. [Online]. Available: https://www.nikon.com/business/fpd/lineup/
[18] B. A. Francis and W. M. Wonham, "The internal model principle for linear multivariable regulators," *Appl. Math. Optim.*, vol. 2, no. 2, pp. 170–194, Jun. 1975.
[19] T. Atsumi, A. Okuyama, and M. Kobayashi, "Track-following control using resonant filter in hard disk drives," *IEEE/ASME Trans. Mechatron.*, vol. 12, no. 4, pp. 472–479, Aug. 2007.
[20] J. Lofberg, "YALMIP : A toolbox for modeling and optimization in MATLAB," in *Proc. IEEE Int. Conf. Robot. Automat.*, 2004, pp. 284–289.
[21] Mosek, "MOSEK 9.3," 2021. [Online]. Available: https://www.mosek.com
[22] S. Skogestad and I. Postlethwaite, *Multivariable Feedback Control*, 2nd ed. Hoboken, NJ, USA: Wiley, 2005.

Masahiro Mae (Member, IEEE) received the B.E., M.S., and Ph.D. degrees in electrical engineering and information systems from The University of Tokyo, Tokyo, Japan, in 2018, 2020, and 2023, respectively.

He is currently an Assistant Professor with the Department of Electrical Engineering and Information Systems, Graduate School of Engineering, The University of Tokyo. His research interests include multivariable control and data-driven learning for mechatronics and energy systems in industrial applications.

Dr. Mae is a Member of Institute of Electrical Engineers of Japan, Society of Instrument and Control Engineers, Society of Automotive Engineers of Japan, and Japan Society of Energy and Resources.

Wataru Ohnishi (Member, IEEE) received the B.E., M.S., and Ph.D. degrees in electrical engineering and information systems from The University of Tokyo, Tokyo, Japan, in 2013, 2015, and 2018, respectively.

He held a visiting position with the Eindhoven University of Technology, Eindhoven, Netherlands. He is currently an Associate Professor with the Department of Electrical Engineering and Information Systems, Graduate School of Engineering, The University of Tokyo. His research interests include high-precision motion control and optimization.

Dr. Ohnishi is a Senior Member of the Institute of Electrical Engineers of Japan.

Hiroshi Fujimoto (Fellow, IEEE) received the Ph.D. degree in electrical engineering from The University of Tokyo, Tokyo, Japan, in 2001.

In 2001, he joined the Department of Electrical Engineering, Nagaoka University of Technology, Niigata, Japan, as a Research Associate. From 2002 to 2003, he was a Visiting Scholar with the School of Mechanical Engineering, Purdue University, West Lafayette, IN, USA. In 2004, he joined the Department of Electrical and Computer Engineering, Yokohama National University, Yokohama, Japan, as a Lecturer, and became an Associate Professor in 2005. From 2010 to 2020, he was an Associate Professor with The University of Tokyo, where has been a Professor since 2021. His interests include control engineering, motion control, nanoscale servo systems, electric vehicle control, motor drive, visual servoing, and wireless power transfer.

Dr. Fujimoto is a Senior Member of Institute of Electrical Engineers of Japan. He is also a Member of the Society of Instrument and Control Engineers, Robotics Society of Japan, and Society of Automotive Engineers of Japan. He was the recipient of the Best Paper Award from IEEE TRANSACTIONS ON INDUSTRIAL ELECTRONICS in 2001 and 2013, Isao Takahashi Power Electronics Award in 2010, Best Author Prize of SICE in 2010, the Nagamori Grand Award in 2016, First Prize Paper Award for IEEE TRANSACTIONS ON POWER ELECTRONICS in 2016, and IEEJ Industry Applications Society Distinguished Transaction Paper Award in 2018 and 2023. He has been a Senior Editor for IEEE/ASME TRANSACTIONS ON MECHATRONICS since 2022 and an Associate Editor for the *IEEE Industrial Electronics Magazine* since 2006. He has been a Chairperson of the Society of Automotive Engineers of Japan (JSAE) Technology Board since 2022 and was a past Chairperson of the IEEE/IES Technical Committee on Motion Control from 2012 to 2013, and the JSAE vehicle electrification committee from 2014 to 2020.

Koichi Sakata received the B.S., M.S., and Ph.D. degrees in physics, electrical, and computer engineering from Yokohama National University, Yokohama, Japan, in 2006, 2008, and 2011, respectively.

He was a Research Student with The University of Tokyo, Tokyo, Japan, from 2010 to 2011. He was also a Research Fellow (DC2) of Japan Society for the Promotion of Science, from 2009 to 2011. Since 2011, he has been with Nikon Corporation, Yokohama, Japan. His research interests include motion control and nano-scale servo control. He works on the design of a motion control and high-precision servo control of large-scale stage.

Dr. Sakata is a Senior Member of the Institute of Electrical Engineers of Japan.